*minerals*

MDPI

*Article*

# The Miocene Source-to-Sink Evolution of Fibrous Clay Minerals in Hyperalkaline Playa-Lakes, Duero Basin (Central Spain)

**Pablo del Buey [1,2,3,*], María Esther Sanz-Montero [3], Juan Pablo Rodríguez-Aranda [3,4], Mónica Sánchez-Román [1] and Fernando Nieto [2]**

[1] Geobiology Laboratory, Department of Earth Sciences, Faculty of Science, Vrije Universiteit Amsterdam, De Boelelaan 1100, 1081 HZ Amsterdam, The Netherlands; m.sanchezroman@vu.nl
[2] Department of Mineralogy and Petrology, Faculty of Science, University of Granada, Avda. de Fuente Nueva, s/n, 18071 Granada, Spain; nieto@ugr.es
[3] Department of Mineralogy and Petrology, Faculty of Geological Sciences, Complutense University of Madrid, C/Profesor José Antonio Novais 12, 28040 Madrid, Spain; mesanz@ucm.es (M.E.S.-M.); juanparo@ucm.es (J.P.R.-A.)
[4] IES Camilo José Cela, Av. Monte, 16, Pozuelo de Alarcón, 28223 Madrid, Spain
* Correspondence: pablodelbuey@ucm.es

**Abstract:** Palygorskite is assumed to be the predominant clay mineral in playa-lakes, where it may be detrital or authigenic in origin. Discriminating between detrital and authigenic clays is crucial to elucidate paleoenvironmental conditions in lacustrine deposits. This study provides insight into the sedimentary evolution of clay minerals from source, lacustrine Miocene marlstones and mudstones, to sink, represented by three recent hyperalkaline playa-lakes in Central Spain. XRD, TEM, and AEM analyses show concomitant detrital and authigenic palygorskites in the three playa-lakes. The inherited palygorskites exhibit degradation features, larger widths, and common and ideal compositions, in contrast to neoformed particles. The latter are narrower. Depending on the hydrochemical composition of each playa-lake, neoformed palygorskites are enriched in a different octahedral cation ($Al_2O_3$, MgO, and $Fe_2O_3$). Iron-rich palygorskites are only formed in association with authigenic saponites in one of the playa-lakes. The same effect of magnesium competition between smectite and palygorskite is observed in Miocene mudstones, where palygorskite is relatively enriched in iron. In hyperalkaline, seasonal playa-lakes lying in the vicinity, slight physicochemical differences play a crucial role in the crystallochemical composition of authigenic palygorskites, highlighting the use of this mineral as a geochemical proxy.

**Keywords:** TEM-AEM; palygorskite; chlorite; mudstones; marlstones; sedimentation

Academic Editor: Harald G. Dill

Received: 5 November 2024
Revised: 28 December 2024
Accepted: 31 December 2024
Published: 3 January 2025

**Citation:** del Buey, P.; Sanz-Montero, M.E.; Rodríguez-Aranda, J.P.; Sánchez-Román, M.; Nieto, F. The Miocene Source-to-Sink Evolution of Fibrous Clay Minerals in Hyperalkaline Playa-Lakes, Duero Basin (Central Spain). *Minerals* **2025**, *15*, 50. https://doi.org/10.3390/min15010050



## 1. Introduction

The occurrence of the fibrous clay minerals, palygorskite, and sepiolite in lacustrine rocks has been widely reported in the literature [1–3]. Fibrous clay minerals can precipitate from multiple mechanisms. Sepiolite is a common neoformed mineral precipitated from a colloidal silicate precursor in magnesium-rich environments via desiccation [4]. Palygorskite can precipitate from aluminic precursors [5,6] and directly from dissolution [7,8]. Ref. [9] revealed that the desiccation of gel precursors is responsible for the textural features of palygorskite and sepiolite in Miocene palustrine facies at Nullarbor Plain

(Australia). More recently, microbially induced palygorskite neoformation has been recognized in hypersaline playa-lakes in relation to desiccated extracellular polymeric substances within microbial mats [10].

The transformation of pre-existing clay minerals (e.g., chlorite, illite, stevensite, and kerolite) is another common mechanism of palygorskite and sepiolite formation [11–13]. Detrital clay minerals in lacustrine environments usually exhibit textural features related to degradation (i.e., weathering and loss of elements) due to reworking under new hydrochemical conditions [14]. Detrital clay minerals in playa-lake systems consist of mixtures of clay minerals, mainly illite, kaolinite, and dioctahedral smectite [2], which contribute to the precipitation of magnesium smectite. In environments where detrital clay minerals are present in low proportions, the purer magnesium phyllosilicates, sepiolite and kerolite, can precipitate [15].

In the case of neoformation, supersaturation is the fundamental control of authigenic clay mineral precipitation [16]. Ref. [5] summarized the physicochemical parameters of sepiolite and palygorskite neoformation. These environmental parameters were high alkalinity (pH around 8–9.5), high Mg+Fe/Si ratios, and low $P_{CO2}$ between water and sediment. In addition, the stability of palygorskite and sepiolite is a function of pH, which the latter is unstable at pH ≥ 12. In waters that are not in equilibrium with atmospheric $CO_2$, the effect of $P_{CO2}$ is less obvious due to its effect on pH value [17]. Finally, a significant increment in the $CO_2$ concentration, biotic or abiotically induced, could result in the dissolution of magnesium clay minerals [18].

Among others, two Cenozoic continental basins of Central Spain, the Madrid and Duero Basins, are well-known to bear palygorskite-rich lacustrine and palustrine facies associated with alluvial fan systems in transition to lacustrine environments [11,19–21]. In some intervals of the intermediate Miocene unit of the Madrid Basin [22,23], sepiolite is abundant enough to be economically exploited in open-pit mines. The extra-basin source of magnesium required for the precipitation of neoformed sepiolite is still a subject of debate [24]. In the Duero Basin, the deposition of palygorskite is commonly linked to the transformation of detrital phyllosilicates in relation to alluvial fans [11,25].

The aim of this investigation is to analyze the depositional processes of authigenic and clastic fibrous clay minerals and the associated clays in modern hyperalkaline playa-lakes under variable hydrochemical conditions. The transport of clays from Miocene lacustrine sources into the new environment involves physicochemical changes. The results show that there are two distinct populations of fibrous clay minerals in playa-lakes, one of detrital origin and the other of neoformed palygorskites. In each playa-lake, neoformed palygorskites and sepiolites are enriched in an octahedral cation (MgO, $Al_2O_3$, and $Fe_2O_3$) in comparison to Miocene fibrous clay minerals. The specific enrichment in one or another of the cations is controlled by the interplay of dissolution, precipitation, and transformation processes.

## 2. Geological Setting

The Caballo Alba, Las Eras, and Bodón Blanco lakes are located in the Coca–Olmedo endorheic wetland in the southwestern sector of the Duero Basin (Central Spain) (Figure 1 up). The three playa-lakes overlie horizontally bedded Miocene and Quaternary deposits in the Duero Basin (Figure 1 down). The Miocene sediments in the vicinity of Caballo Alba lake (Figure 1 down) consist of gray-greenish marlstones, dolo-marlstone, and mudstones [26]. Miocene facies are deposited in the marginal subenvironments of saline lakes belonging to the Cuestas Unit [27]. Quaternary conglomerates, sandstones, and siltstones were deposited in the fluvial systems running through the study area (Figure 1 down) [28].

Caballo Alba, with a maximum area of 0.17 $km^2$, is a shallow basin (up to 0.5 m deep) fed by groundwater [26]. In addition, low water inputs were derived from a small,

extremely ephemeral stream. Caballo Alba presents high pH values ranging from 9.0 to 10.4, thus presenting brackish-to-saline water (1–16 $g \cdot L^{-1}$), whereas Las Eras reached the highest pH value recorded, "up to 11.3". Overall, the hydrochemical composition of Caballo Alba, Las Eras, and Bodón Blanco is characterized by high carbonate concentrations, with chloride dominant over sulfate. Nevertheless, the hydrochemical composition is very variable among the playa-lakes: the analysis of most of the data mainly shows $Na^+$-$Cl^-$ composition, but some values correspond to $Na^+$-$Cl^-$-$SO_4^{2-}$-$HCO_3^-$ for Caballo Alba and Las Eras. Bodón Blanco hydrochemistry is classified into three different areas of the Piper–Hill–Langelier diagram, including $Na^+$-$HCO_3^-$ [29]. Finally, the concentration of dissolved potassium is an order of magnitude higher in Las Eras than in Caballo Alba and Bodón Blanco [30].

The region is characterized by a continental Mediterranean climate, with low mean annual rainfall of 400–500 $mm \cdot year^{-1}$ and average temperatures of 13 °C [29]. Mostly from March to May, the Caballo Alba playa-lake hosts benthic and floating microbial mats that expand over the lake (Figure 2A,B). In spring, macroscopic filamentous green algae of the genus *Spirogyra* become entangled with *Cyanobacteria* (*Oscillatorya* genus) and Diatoms (Figure 2B) [31]. The lake is also colonized by charophyte and the associated ostracod biota. Eventually, the photosynthetic activity of some microbes produces oxygen bubbles that detach benthic microbial mats, which float and rise to the surface [32]. Ref. [31] described the intracellular precipitation of calcite and dolomite during the conjugation cycle of *Spirogyra*. Calcite and dolomite are the most abundant carbonates in these hyperalkaline playa-lakes. From June to October, coinciding with periods of low rainfall, the lake floor dries out and Caballo Alba, Las Eras, and Bodón Blanco become playas covered by a white mineral crust (Figure 2A,C). The crust contains an assemblage of authigenic carbonates (e.g., calcite, dolomite, nesquehonite, hydromagnesite, natron, and trona), sulfates (e.g., hexahydrite, starkeyite, gypsum, thenardite, and bloedite), chlorides (halite), and magnesium clays (Figure 2C) [26,29]. Some magnesium carbonates like hydromagnesite, magnesite, and huntite can precipitate due to the heterotrophic degradation of microbial mass [33]. Underneath the desiccated microbial mat mass, some quartzite pebbles, cobbles, and boulders were bound and trapped (Figure 2D).

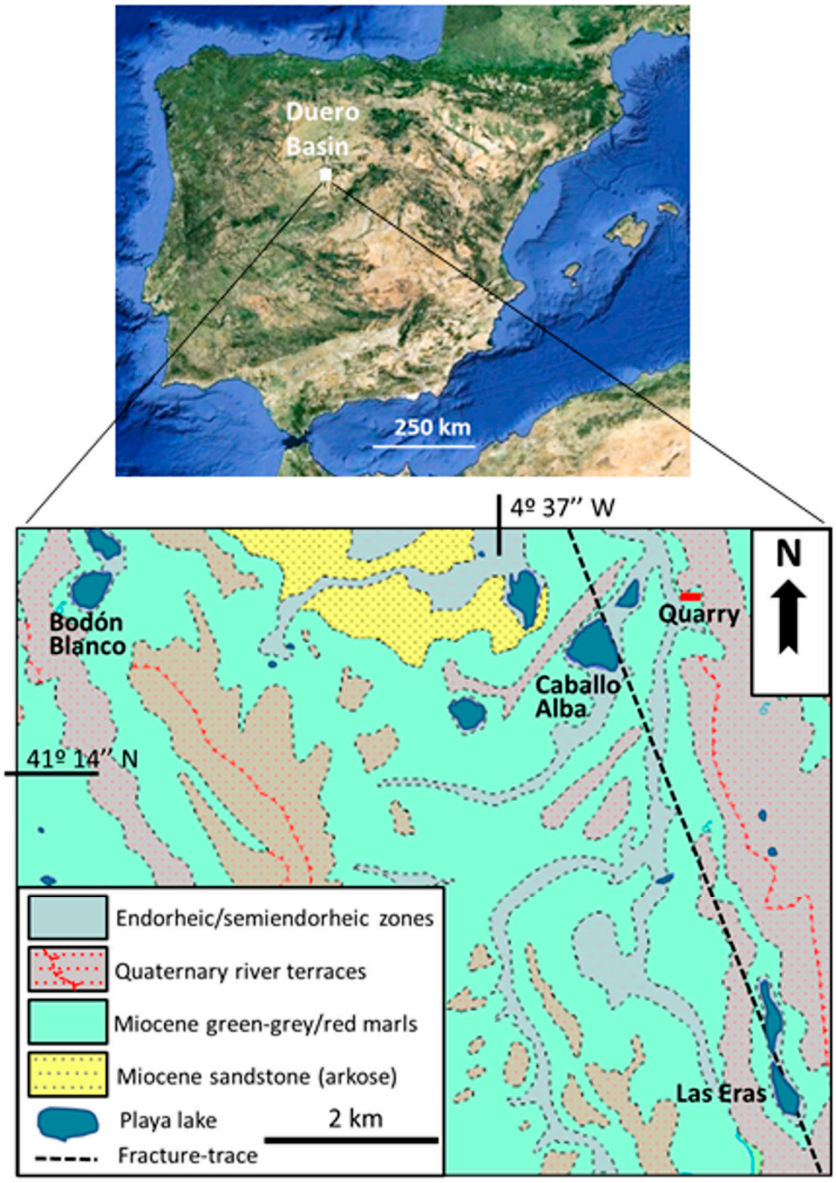


**Figure 1.** Location of the study area: (**up**) satellite image (source of the image Google Earth); (**down**) geological map (based on MAGNA 1:50.000, n° 428) showing the location of the Caballo Alba, Las Eras, and Bodón Blanco playa-lakes.

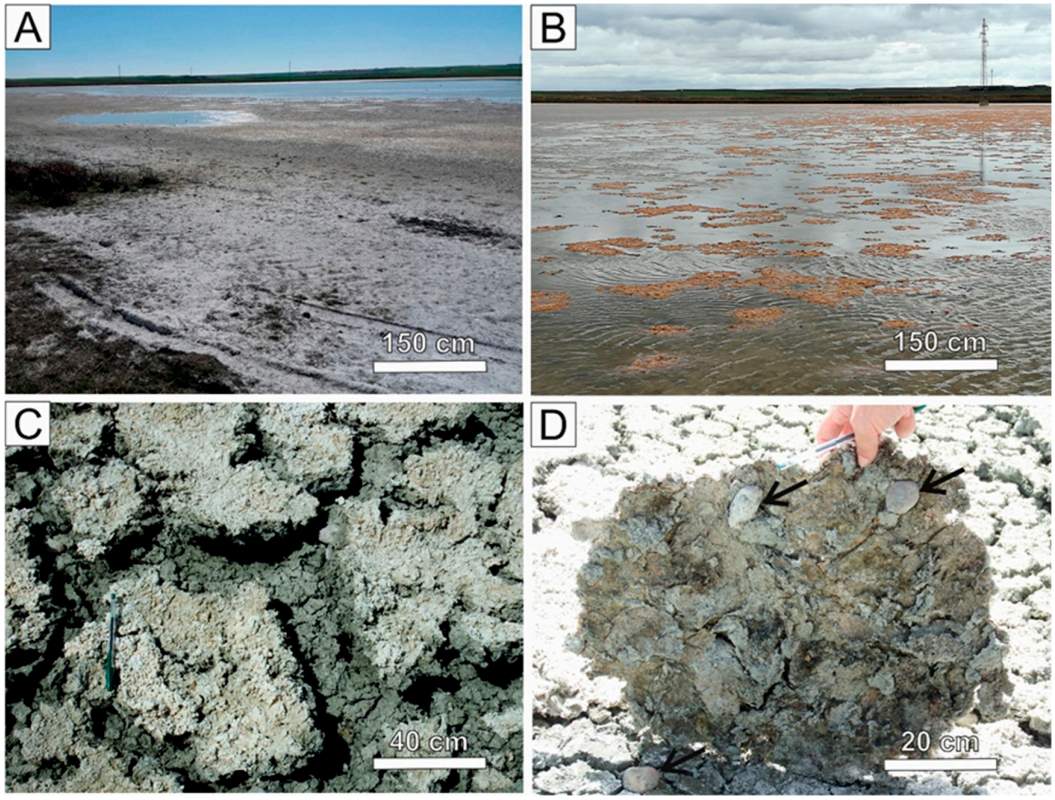


**Figure 2.** Sedimentary evolution in the Caballo Alba playa-lake: (**A**) white mineral precipitates (e.g., hydromagnesite, northupite, natron, and trona, among others) on the shore and in ponds during desiccation; (**B**) floating microbial mats during the wet season (December 2018); (**C**) desiccation cracks in the sediment (July 2020); (**D**) quartzite pebbles, cobbles, and boulders trapped beneath a desiccated microbial mat (black arrows).

### *2.1. Playa-Lake Sediments*#

Twenty-six surface sediment samples comprising mineral and organic matter from the three playa-lakes were collected at different sites (i.e., located within each playa-lake) and periods (i.e., seasons).

### *2.2. Miocene Deposits*#

Well-exposed outcrops of Miocene rocks surrounding these playa-lakes are scarce. To study the Miocene deposits that constitute the watershed of these playa-lakes, a stratigraphic column was made in a quarry. This small quarry with a height of 10 m (Figures 1 and 3), where common clays are extracted for the ceramic industry (IGME and SIEMCALSA, 2016), is located 1 km NE of Caballo Alba.

The stratigraphic section of Miocene sedimentary rocks is 9.5 m thick, and it is situated at 41°14′58.50″ N//4°35′38.33″ W, lying between 773 m and 783 m.a.s.l. This section consists of marlstones, dolo-marlstones, and mudstones. The different colors in the logged section reflect the colors of these rocks in the outcrop, regardless of their lithology (Figure 3). The lower part of the section is composed of green marlstone up to 2–3 m thick. From 3 to 6.5 m, an alternation of greenish to reddish mudstones is partially covered. From 6.5 to 7 m, there is a whitish marlstone level before a reddish dolo-marlstone level with bioturbation. There is a laminar whitish transition from the reddish dolo-marlstone to the upper 2 m of the brownish-green level of mixed calcitic/dolo-mudstone. At the topmost of the succession is a fluvial channel filled with surrounded quartzite pebbles, cobbles, and boulders [26]. Six marlstone and mudstone samples along the stratigraphic column

were collected in July 2020 (Table S1, Figure 3). Three samples were used for clay mineralogy, TEM, and EDX analyses (Samples 0, 3, and 4).

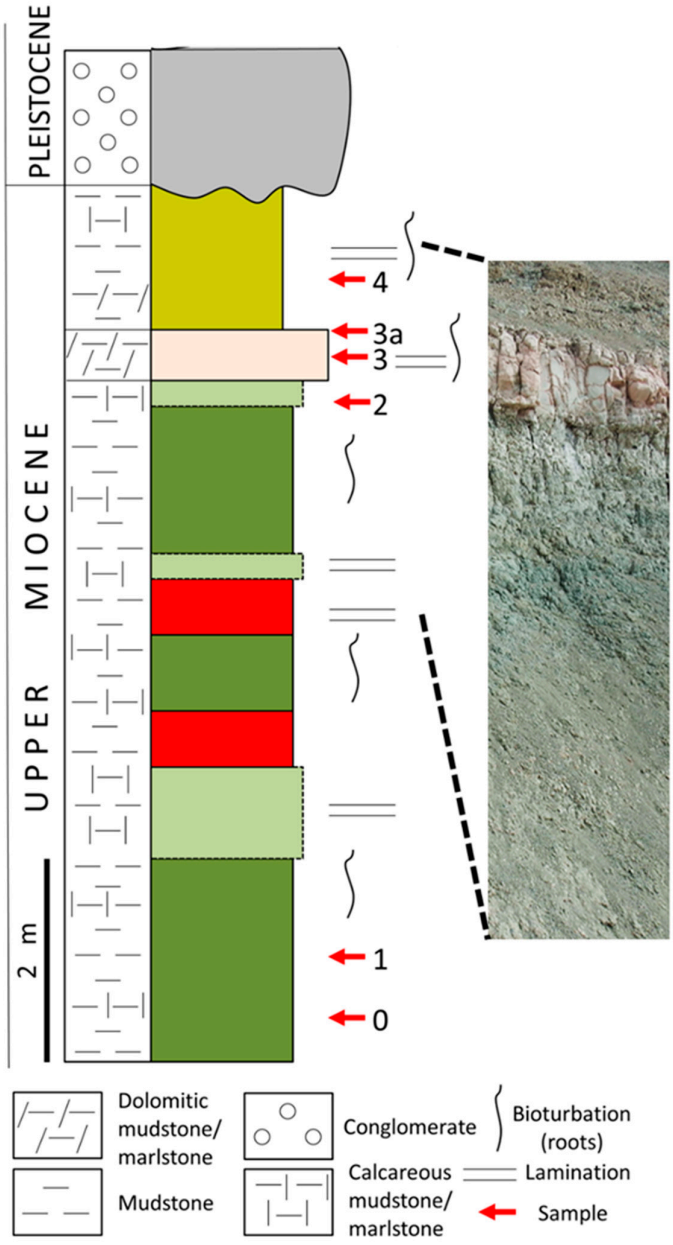


**Figure 3.** Miocene stratigraphic column at the quarry outcrop where marlstone and mudstone samples were collected (0–4). Sample 3a: laminar whitish transition between sample 3 and sample 4.#

## 3. Materials and Methods

### *3.1. Bulk and Clay Mineral Assemblages (XRD)*#

Bulk mineralogy was analyzed by random powder X-ray diffraction (XRD) analysis using a Bruker D8 Advance diffractometer with Cu $K_\alpha$ radiation ($\lambda$ = 1.54060 Å) and equipped with a Sol-X detector. The samples were scanned from 2 to 65° 2θ with a step size of 0.02° 2θ and a counting time of 0.5 s per step. XRD interpretation was based on the method described by [34] using EVA Bruker software (Version 7).

For clay mineralogy analysis, carbonates, sulfates, and organic matter were removed from samples using 200 mL of 0.2 M HCl dissolution and continuously agitated for 20 min

[35,36]. Briefly, a <2 μm fraction of the treated sediment was separated using a centrifuge technique [37] with a Thermo Scientific Sorvall ST 16 Centrifuge (extraction cycles of 1000× *g* during 3 min). Then, the <2 μm fraction was analyzed as oriented mounts prepared by smearing the slurries on glass slides. Three XRD diagrams were obtained for each fraction: after air drying (AD), ethylene glycol solvation (EG), and heating at 550 °C for at least 2 h. These samples were scanned from 2 to 35° 2θ with a step size of 0.02° 2θ and a counting time of 1 s per step. The semiquantification of clay mineral assemblages was performed by using the mineral intensity factor method (MIF) as described in [10]. The names of clay mineral phases were abbreviated according to [38] as follows: mica (Mca), chlorite (Chl), kaolinite (Kln), sepiolite (Sep), palygorskite (Plg), and smectite (Sme).

### *3.2. Textural Features and Crystallochemical Compositions of Fibrous Clay Minerals (TEM-AEM)*

Digital analyses of TEM images are the most effective method for measuring the form of anisotropic particles and distinguishing particle populations within a sample [39]. TEM observations and EDX analyses of 13 samples, 10 of which correspond to playa-lake sediments and 3 of Miocene marlstones (Samples 0, 3, and 4), were obtained from powdered portions prepared using C-coated Cu grids. The TEM data were obtained using two electron microscopes for semiquantitative chemical analyses at the CNME (Complutense University, Madrid, Spain), namely a JEOL 3000F microscope operating at 300 kV and a JEOL JEM 2100 microscope operating at 200 kV. Semiquantitative analyses of particles were performed in the STEM mode using an Oxford Instruments EDX microanalysis system. In order to ensure the reproducibility of the data for quantitative chemical analyses (AEM) of Plg particles from Caballo Alba, data were obtained in the STEM mode using the Thermo Fisher Scientific Talos F200X, operated at 200 kV at the CIC (University of Granada, Granada, Spain). For this task, individual spectra corresponding to each pixel of homogeneous areas were summed up to produce the average spectrum of the entire analyzed area. Albite, biotite, muscovite, spessartine, olivine, and titanite standards were used to obtain K-factors for the transformation of intensity ratios to concentration ratios according to [40,41]. The structural formulae of palygorskite were calculated on the basis of 42 negative charges, i.e., $O_{20}$ $(OH)_2 \cdot (OH_2)_4$. All the Fe was considered as trivalent.

## 4. Results

### *4.1. Miocene Clay Minerals*

The mineralogical clay assemblages of Miocene beds (Figure 4) are composed of Mca, Chl, Kln, Sep, Plg, and Sme. The assemblage comprising Mca-Kln-Plg is ubiquitous across the stratigraphic section, whereas the Chl-Sep-Sme assemblage is irregularly distributed. From bottom to top, the Mca-Chl-Kln-Sep-Plg assemblage is recognized in samples of marlstone and dolo-marlstone. Only the brownish-greenish mixed calcitic/dolo-mudstone has a representative amount of Sme content, as evidenced by the shift in the 001 reflection under ethylene glycol solvation (EG). In this sample, Chl and Sep contents are absent or below the detection limit of the X-ray diffraction technique (<5% wt) (Table S2).

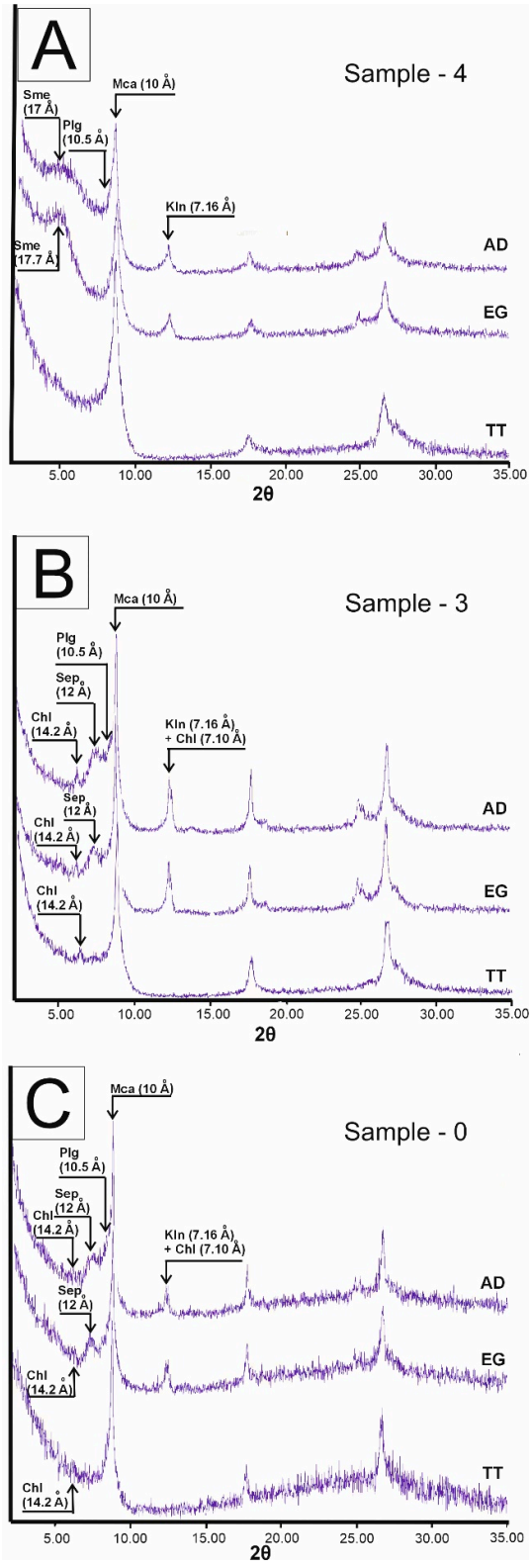


**Figure 4.** XRD patterns of oriented mounts of marlstone and mudstone samples: air-dried (AD), ethylene glycol-solvated (EG), and thermally treated (TT) (550 °C). (**A**) Sample-4: calcitic/dolo-mudstone; (**B**) Sample-3: dolo-marlstones; (**C**) Sample-0: green marlstones.

Textural and Crystallochemical Characterization of Miocen Fibrous Clay Minerals

Textural characterization is based on the width of the Plg fibers and other textural features like length, width/length ratio, fiber curliness, and fiber arrangement [42]. The length and width/length ratios are not described in all images due to the impossibility of completely measuring the length of most fibers in TEM images (Figure 5). Fiber curliness and fiber arrangement were the other key features analyzed. Due to the impossibility of distinguishing between Sep and Plg only by their morphological features [42], crystallochemical analyses of Miocene fibrous clay minerals were performed (Figure 6). X-ray diffraction showed that the most abundant fibrous clay mineral in samples of marlstone and dolo-marlstone is Sep, whereas in calcitic/dolo-mudstone samples, Plg is only present but scarce. In these terms, the fibers from dolo-marlstone are mostly Sep and only Plg for marlstone and calcitic/dolo-mudstone.

The basal unit of the stratigraphic section (Sample 0, Figure 5A–C), which is composed of green marlstones, presents fibers in three different aggregation states (Figure 5): laths (8–17 nm width), rods (12–38 nm width), and bundles (68–69 nm width). These fibers with independent states of aggregation are curved to straight. The basal marlstone bed consists of ideal Plg (Sample 0, Figure 6). The dolo-marlstones in the intermediate interval contain Sep–Plg fibers (Sample 3, Figure 5D–H) in three different aggregation states: laths (9–16 nm), rods (19–45 nm width), and bundles (40–100 nm width). Most fibers in this sample are straight and rigid, whereas rods and bundles are curved (Figure 5G). These clay minerals are classified as common to magnesium Plg (Sample 3, Figure 6). Finally, the brownish-green mixed calcitic/dolo-mudstones at the topmost part of the stratigraphic column present only a few straight Plg laths (8 nm width) (Sample 4, Figure 5I), which are classified as ideal Plg, with higher content of $Fe_2O_3$ (x = 0.4–0.5) than Plg particles comprising the basal marlstones (Sample 4, Figure 6).

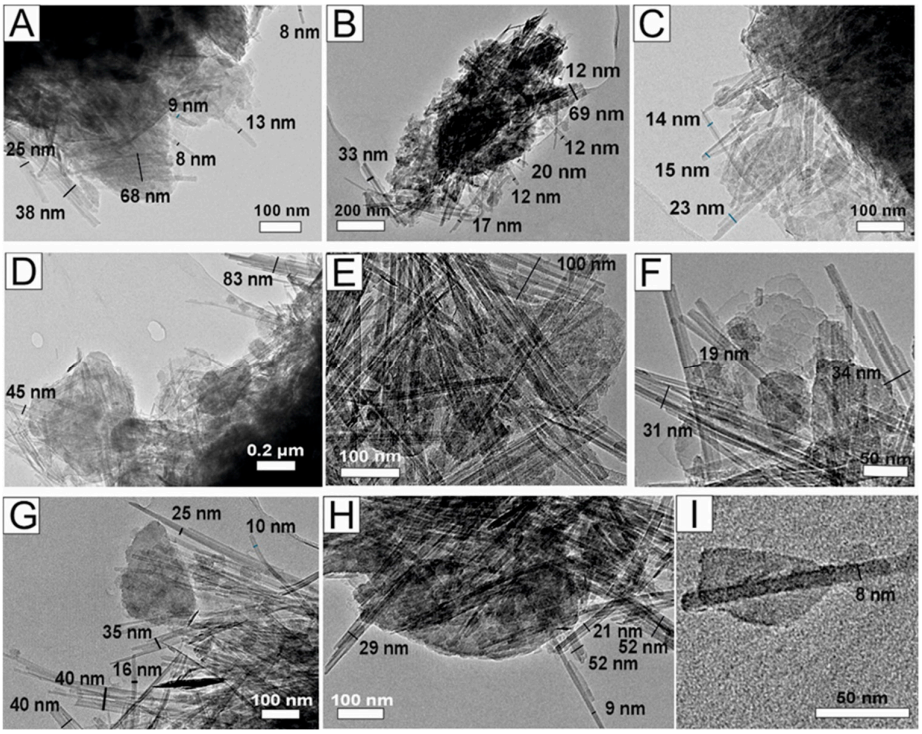


**Figure 5.** TEM micrographs of fibrous clay minerals from Miocene marlstones and mudstone. Sample 0–marlstone (**A–C**): nanometer-sized Sep and minor Plg laths, rods, and bundles from marlstone samples at the base of the sedimentary succession. Sample 3—dolo-marlstone (**D–H**): rods and

bundles of Sep and minor Plg. Sample 4—calcitic/dolo-mudstone (**I**): laths of Plg from the topmost sample from the Miocene sedimentary succession.

The weight percentage results of semiquantitative analyses using TEM-AEM of Plg fibers from the Miocene mudstones and marlstones and the three playa-lakes are plotted in Figure 6. The graph shows that there is no significant variability in the chemical composition. Most of them are plotted in composition fields corresponding to aluminum-rich Plg to common ideal ones, according to [43]. The composition of Miocene fibrous clay minerals is characteristic of each marlstone and mudstone sample. The mean structural formula for Plg marlstone (Sample 0) is $[Si_8O_{20}\ (Mg_2\ Fe_2)_{0.25}\ (Mg_2\ Al_2)\ _{0.75}\ (OH)_2 \cdot (OH_2)_4] \cdot nH_2O$. The dolo-marlstone sample (Sample 3) is characterized by having the most magnesium-rich composition of Plg of the Miocene deposits $[Si_{12}O_{30}Mg_8(OH)_4(OH_2)_2]_{0.1}[Si_8O_{20}\ (Mg_2\ Fe_2)_{0.35}\ (Mg_2\ Al_2)_{0.65}\ (OH)_2\ (OH_2)_4]_{0.9} \cdot n\ H_2O$. The uppermost beds (Sample 4) consist of calcitic/dolo-mudstone with Plg relative enrichment in $Fe_2O_3$ content with the mean structural formula $[Si_8O_{20}\ (Mg_2\ Fe_2)_{0.45}\ (Mg_2\ Al_2)_{0.55}\ (OH)_2 \cdot (OH_2)_4] \cdot nH_2O$.

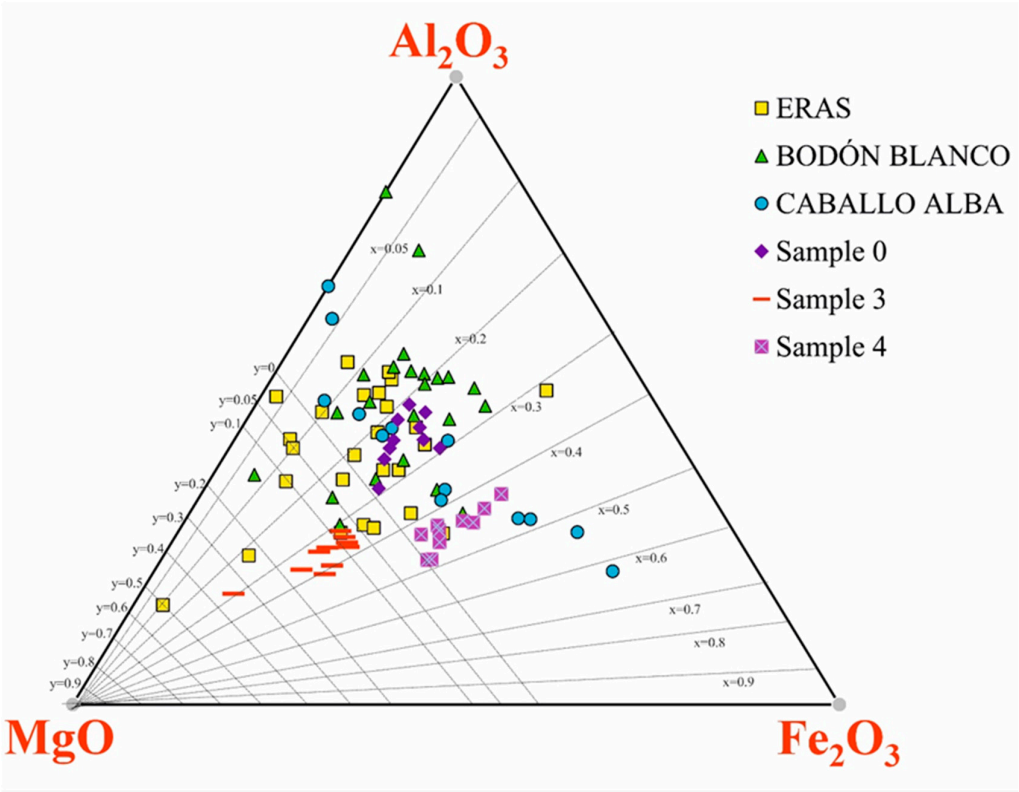


**Figure 6.** AEM analyses of Plg in the Miocene and playa-lakes deposits, plotted in a ternary graph, modified from [43].

### *4.2. Clay Mineralogy of the Playa-Lakes*

The surface sediment samples and microbial mats that proliferate in these three playa-lakes were characterized in terms of clay mineralogy. The clay mineralogy assemblage of Caballo Alba comprises Mca, Plg, Sme, and Kln. In addition, Sep is irregularly distributed and is always below 10% in relative abundance. Sme is always present, with remarkably higher relative abundances (up to 45%) than those of the Miocene strata (Figure 7, Table S3), as well as the Las Eras and Bodón Blanco playa-lake deposits. The sediments of the Las Eras playa-lake lack Sme (Figure S1, Table S4), whereas in the Bodón

Blanco playa-lake, Sme represents up to 10% of the clay mineral assemblage (Figure S2, Table S5).

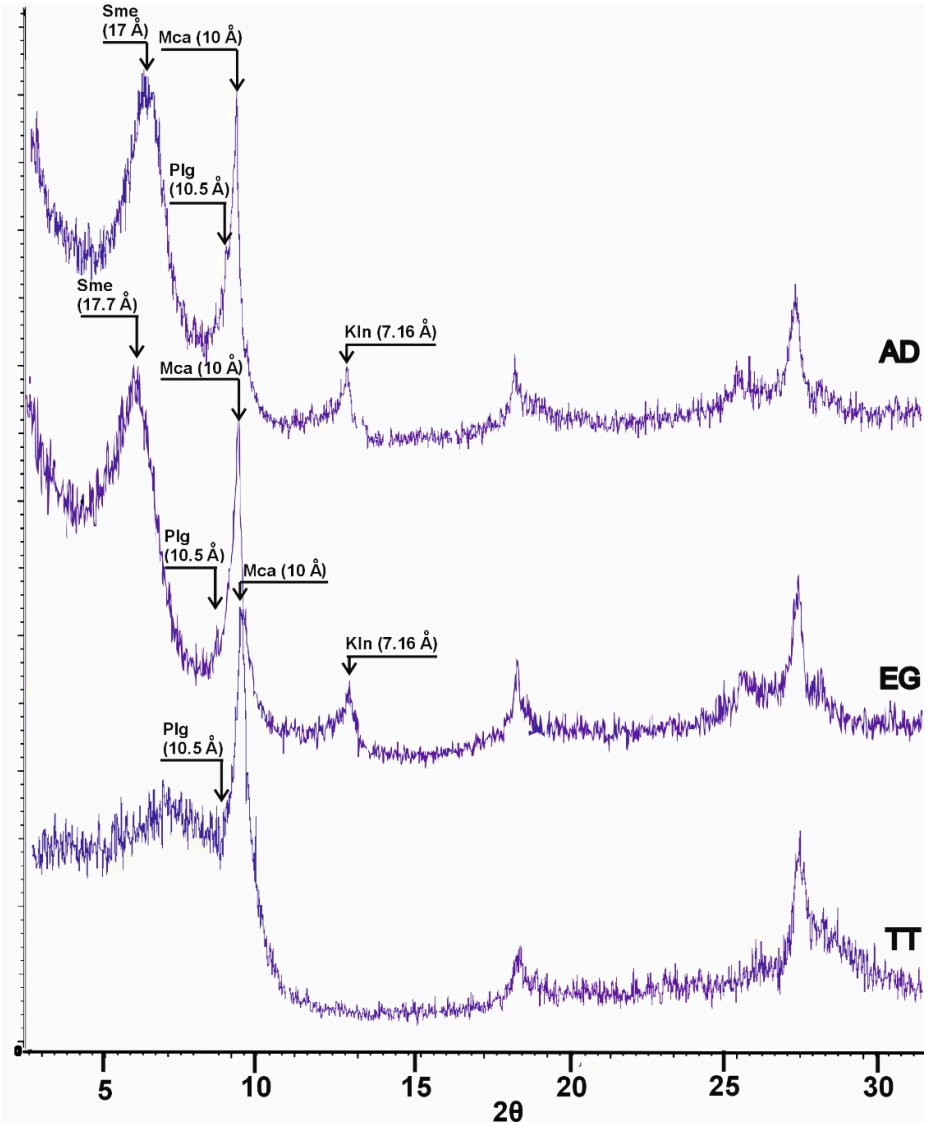


**Figure 7.** XRD patterns of oriented mounts of a desiccated microbial mat from the Caballo Alba playa-lake: air-dried (AD), ethylene glycol-solvated (EG), and thermally treated (TT) (500 °C).

4.2.1. Textural and Crystallochemical Characterization of Fibrous Clay Minerals from Playa-Lakes

Fibrous clay minerals (mostly Plg) were classified according to crystallochemical classification by [43]. In this sense, there are three different groups of Plg particles according to their enrichment with some octahedral cations: $Al_2O_3$ (Figure 8), $Fe_2O_3$ (Figure 9), and MgO (Figure 10). Plg with intermediate compositions, which are the majority of these minerals, are shown in Figure 11. In the corners of the ternary diagram, the Plg particles from the three playa-lakes enriched in one of the octahedral cations $Al_2O_3$, MgO, or $Fe_2O_3$ are shown (Figure 6). Notably, a group of Plg from Caballo Alba are enriched in $Fe_2O_3$ $[Si_8O_{20}$ $(Mg_2$ $Fe_2)_{0.6}$ $(Mg_2$ $Al_2)_{0.4}$ $(OH)_2 \cdot (OH_2)_4]\cdot nH_2O$, while some minor particles corresponding to Las Eras and Bodón Blanco can be classified as magnesium-rich Plg/aluminum-rich Sep $[Si_{12}O_{30}Mg_8(OH)_4(OH_2)_2]_{0.5}[Si_8O_{20}$ $(Mg_2$ $Fe_2)_{0.1}$ $(Mg_2$ $Al_2)_{0.9}$ $(OH)_2 \cdot (OH_2)_4]_{0.5}\cdot nH_2O$. Most aluminum-rich Plg $[Si_8O_{20}$ $(Mg_2$ $Fe_2)_0$ $(Mg_2$ $Al_2)_1$ $(OH)_2 \cdot$

$(OH_2)_4]_1 \cdot nH_2O$ minerals correspond to the particles of Bodón Blanco. The four varieties of Plg particles are described next in terms of width, curliness, and arrangement of the fibers (Table S2).

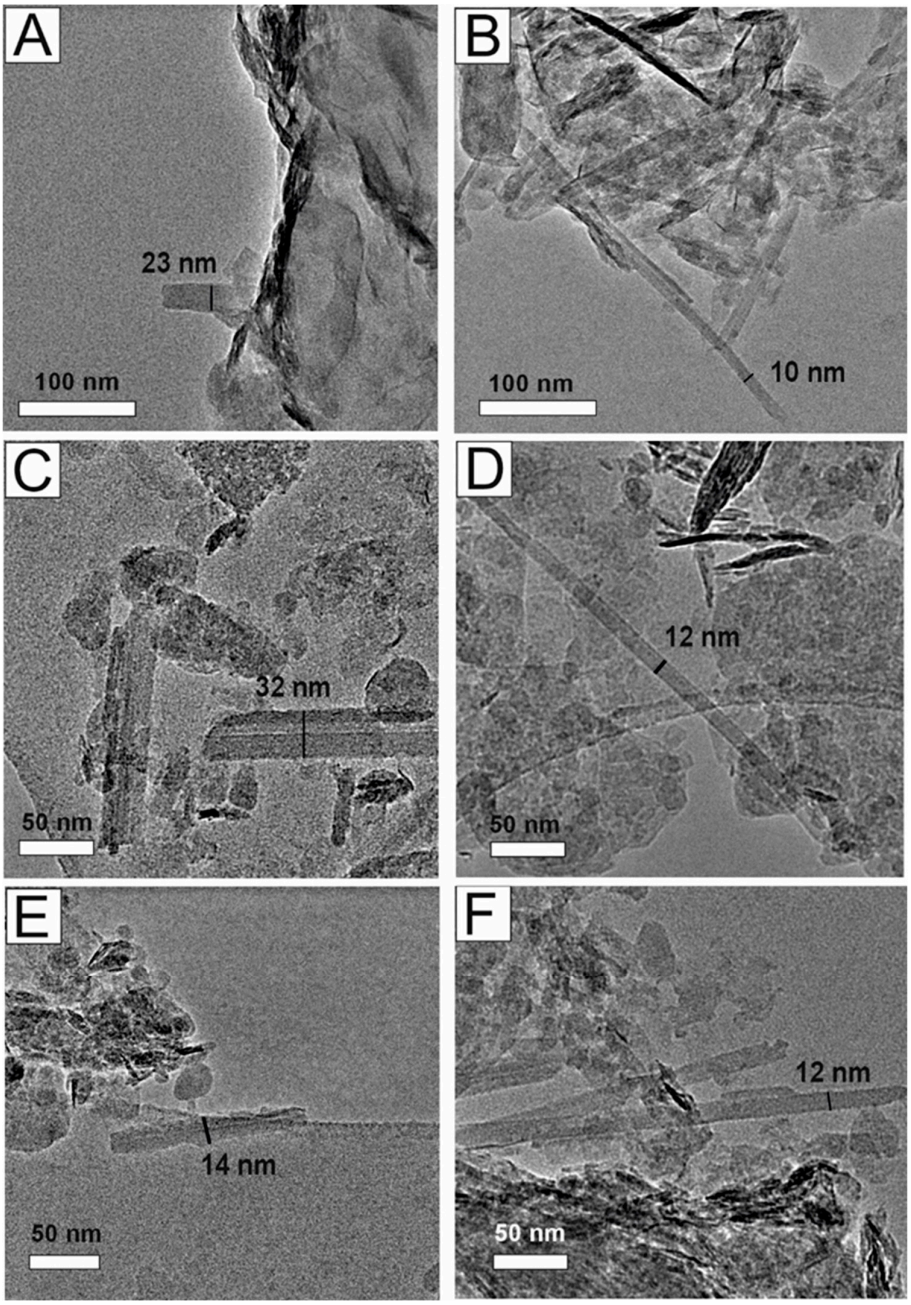


**Figure 8.** Aluminum-rich Plg fibers deposited in the playa-lakes: Bodón Blanco (**A**–**C**), Caballo Alba (**D**,**E**), and Las Eras (**F**): (**A**) Plg lath associated with particles of Sme; (**B**) Plg lath; (**C**) Plg rods; (**D**–**F**) Plg lath.

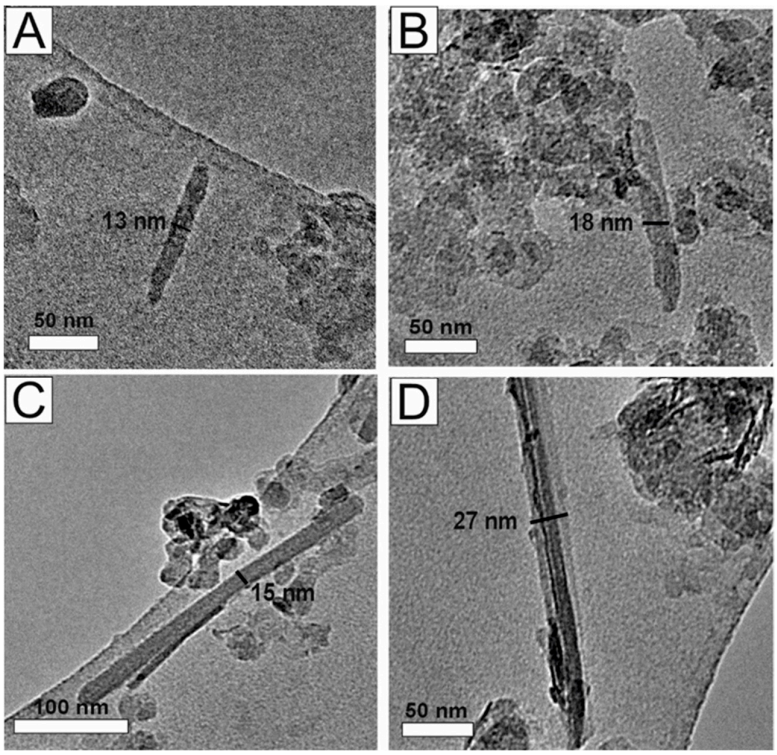


**Figure 9.** Iron-rich Plg from the Caballo Alba playa-lake: (**A**) nanometer-sized Plg particle; (**B**) Plg lath shorter than 100 nm; (**C**) Plg lath longer than 100 nm; (**D**) Plg rod.

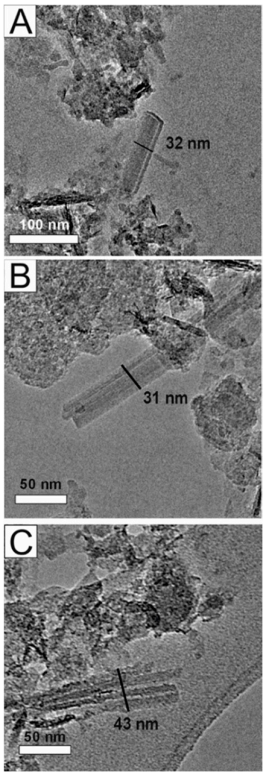


**Figure 10.** Magnesium Plg and aluminum Sep from the Las Eras playa-lake: (**A**) rod of aluminum Sep, 100 nm in length; (**B**) rod of aluminum Sep; (**C**) bundle of magensium Plg.

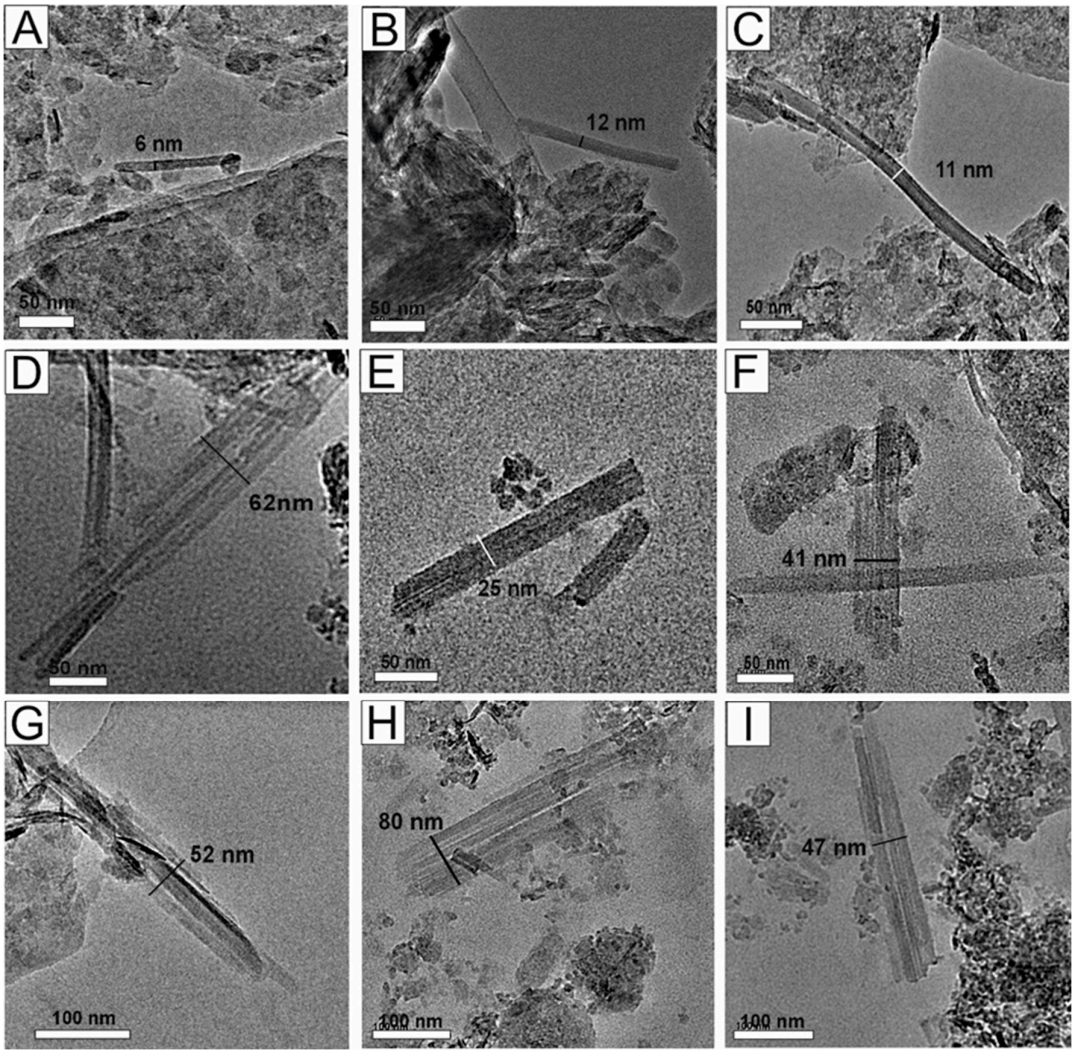


**Figure 11.** Intermediate composition Plg deposited in the playa-lakes: Caballo Alba (**A**), Las Eras (**B**–**I**), and Bodón Blanco (**G**): (**A**) nanometer-sized Plg lath; (**B**,**C**) Plg laths; (**D**–**I**) partially degraded bundles of Plg.

### Aluminum-Rich Plg

Aluminum-rich Plg particles are recognized in the three studied hyperalkaline playa-lakes. In Bodón Blanco (Figure 8A–C), Plg consists of lath and rods enriched in $Al_2O_3$ (20.17%–27.95% wt). The width of Plg particles varies from 10 nm of laths to 23–32 nm of rods. The laths of Plg (Figure 8D–E) in Caballo Alba range from 21.06 to 25.54% wt of $Al_2O_3$. The width of the laths of Plg particles varies from 12 to 14 nm. Las Eras aluminum-rich Plg laths (21.57% wt) are scarce and present widths of 12 nm (Figure 8F). Many of these particles are straight and rigid (Figure 8A,C,E,F), and only a few of them are curved (Figure 8B,D).

### Iron-Rich Plg

Iron-rich Plg particles are only found in the Caballo Alba playa-lake (Figure 9). In relation to their length, two populations of fibers can be distinguished. The smallest laths are up to 100 nm in length (Figure 9A,B). By contrast, the larger fibers, laths (13–18 nm width), and rods (27 nm width) are more than 100 nm in length. All these Plg fibers are straight and rigid. The content of $Fe_2O_3$ of these Plg is particularly high (10.40%–21.71% wt).

The results of quantitative TEM-AEM analyses of Plg from Caballo Alba and their structural formulae were obtained from one sample (Table 1). According to the Plg crystallochemical classification established by [44], three types of Plg can be distinguished in terms of the number of Mg atoms per half unit cell (p.h.u.c) vs. the number of octahedral positions occupied (p.h.u.c): types II, III and IV. The results of the structural formulae for iron-rich Plg are highlighted in green. Type IV represents aluminum-rich Plg. Maximum, minimum, and mean values for each tetrahedral, octahedral, interlayer, and the sum of octahedral cations are presented in Table 1.

**Table 1.** Structural formulae proposed for the studied Plg from the Caballo Alba playa-lake.

| Sample | Si | $^{IV}$ Al | $^{VI}$ Al | Mg | $Fe^{3+}$ | ∑OC | Ca | K | Na | Type |
|---|---|---|---|---|---|---|---|---|---|---|
| CA I/01 | 7.4 | 0.6 | 1.41 | 2.19 | 0.47 | 4.07 | 0.1 | 0.23 | 0.14 | Type II |
| CA I/02 | 7.45 | 0.55 | 1.09 | 2.55 | 0.49 | 4.13 | 0.09 | 0.32 | 0.17 | Type III |
| CA I/03 | 7.10 | 0.9 | 0.88 | 2.88 | 0.64 | 4.4 | 0.07 | 0.29 | 0.16 | Type III |
| CA I/04 | 7.36 | 0.64 | 0.53 | 3.37 | 0.38 | 4.28 | 0.21 | 0.11 | 0.64 | Type III |
| CA I/05 | 7 | 1 | 0.57 | 2.78 | 0.8 | 4.15 | 0.21 | 0.19 | 0.72 | Type III |
| CA I/06 | 6.94 | 1.06 | 0.74 | 3.54 | 0.42 | 4.7 | 0.05 | 0.25 | 0.15 | Type III |
| CA I/07 | 7.21 | 0.79 | 0.82 | 3.57 | 0.31 | 4.7 | 0.09 | 0.07 | 0.03 | Type III |
| CA I/08 | 7.23 | 0.77 | 1.6 | 1.46 | 0.51 | 3.57 | 0.23 | 0.51 | 0.55 | Type IV |
| CA I/09 | 6.68 | 1.32 | 1.29 | 1.35 | 0.74 | 3.38 | 0.52 | 0.61 | 0.86 | Type IV |
| CA I/10 | 7.47 | 0.53 | 2.18 | 0.7 | 0.43 | 3.31 | 0.13 | 0.82 | 0.24 | Type IV |
| CA I/11 | 7.35 | 0.65 | 2.23 | 0.85 | 0.34 | 3.42 | 0.12 | 0.71 | 0.3 | Type IV |
| | | | | | | | | | | |
| MAX | 7.47 | 1.32 | 2.23 | 3.57 | 0.8 | 4.7 | 0.52 | 0.82 | 0.86 | |
| MIN | 6.68 | 0.53 | 0.53 | 0.7 | 0.31 | 3.31 | 0.07 | 0.07 | 0.03 | |
| MEAN | 7.20 | 0.80 | 1.21 | 2.29 | 0.50 | 4.01 | 0.17 | 0.37 | 0.36 | |

Magnesium Plg and Aluminum Sep

Magnesium-rich Plg and aluminum Sep particles are found in the Las Eras playa-lake (Figure 10). The state of the fiber arrangement varies from rods (31–32 nm width) to bundles (43 nm width), from straight and rigid to curved. The MgO content ranges from 20.23% to 27.79% wt.

Common and Ideal Plg

This group of minerals is the most representative in terms of the number of particles analyzed (Figure 11). The compositional limits can be established in the ternary diagram by the "y" and "x" values. The "y" value corresponds to the proportion of Sep and Plg polysomes [43], whereas "x" indicates the $Fe_2O_3$ content in Plg polysomes. In this line, "y" values vary from 0.1 beyond to 0, and "x" varies from 0.1 to 0.4. This implies that all Plg particles in this field can be mostly classified as common and ideal Plg particles [43].

There are two populations of fibrous clay minerals among the three playa-lakes: laths of Plg (6 nm to 12 nm widths) (Figure 11A–C) and partially degraded rods and bundles of Plg (25 nm to 62 nm widths) (Figure 11D–I). Another textural difference between these two populations is the fiber curliness: laths are curved (Figure 11A–C), whereas partially degraded rods and bundles are straight and rigid (Figure 11D–I).

## 5. Discussion

The mineralogical, textural, and chemical analyses provide supporting evidence indicating that a mixed assemblage of detrital and authigenic Plg is deposited in the three hyperalkaine playa-lakes studied. The crystallochemical compositions of the detrital Plg particles analyzed are equivalent to Miocene marlstones and mudstones. Alternatively, authigenic Plg particles, and to a minor extent aluminum Sep, are characterized by greater proportions of octahedral cations ($Al_2O_3$, MgO, and $Fe_2O_3$) in the playa-lakes. High pH and minor differences in the geochemical compositions of the studied playa-lakes influence the precipitation of different types of Plg as well as the precipitation of Sme and the dissolution of Chl. The authigenic processes of iron-rich Plg precipitation are closely associated with the Caballo Alba playa-lake and Miocene calcitic/dolo-mudstone, where Plg is present along with Sme content.

Plg deposited in recent lacustrine environments is commonly detrital [1]. A similar interpretation applies to most of the Plg deposited in the three studied playa-lakes. Due to the shallow nature of these playa-lakes and their surface area, Plg was homogeneously distributed throughout the lakes. The small particle size also favors the transport of clay minerals in suspension from one area to another [45]. Plg particles migrate and move preferentially over Sme and Kln [46]. Rods and bundles of detrital Plg are straight and rigid and close to the ideal composition (Figure 10A–C). The widths measured in the detrital bundles of Plg in these playa-lakes, ranging from 25 to 80 nm, have been also reported in Plg fibers deposited in other worldwide geological settings [47–49].

In relation to mineralogy, the crystallochemical composition and textural features, including width, fiber curliness, and the arrangement of Plg fibers deposited in modern lakes, fit well with the features of fibrous clay minerals forming the Miocene strata in the watershed [26]. There are many examples of detrital Plg deposits and their parent rocks in different geological formations worldwide [50–52].

Our results show that these alterations of detrital clay minerals and the precipitation of authigenic ones are related to the high pH values that these playa-lakes consistently record. As the pH increases, the separation and dispersion degrees of Plg fibers increase, whereas the contents of $SiO_2$, $Al_2O_3$, MgO, and $Fe_2O_3$ in Plg remain constant [53]. On the edges of these fibers, degradation is evident. Plg is stable only at high pH values [7]. There is no significant variation with the increase in pH value (i.e., up to 13), neither at the $d_{110}$ peak intensity nor at the full width at half maximum [53]. In addition, Sep is more abundant than Plg in the studied Miocene marlstones, whereas Plg is more abundant in the hyperalkaline lakes studied. Although Sep is a mineral with low solubility, its long-term interaction with hyperalkaline waters (i.e., $8 > pH < 13$) results in a greater decrease in the length of Sep fibers and subsequent dissolution of Si-OH groups than those reported by [54].

A second population of fibrous clay minerals is considered authigenic because of their notable differences in composition and texture, with regard to the detrital, concerning width, and particle aggregation. The measured widths of these neoformed Plg fibers range from 6 to 32 nm. Similar ranges of widths are common in neoformed Plg [55,56] and [6]. Plg and Sep are clay minerals that are typically formed in lacustrine evaporitic environments [1], where Plg predominates over other clay minerals, especially in mudflats and playa-lakes [2]. Consequently, Plg formation in sedimentary environments can be controversial, as it is either inherited from source areas or authigenic [57]. Those authigenic Plg and Sep fibers distinctly consist of laths and rods enriched with octahedral cations $Al_2O_3$, MgO, or $Fe_2O_3$ (Figures 8–10). The composition of a minority of authigenic Plg is closer to common and ideal terms (Figure 11A–C). Overall, neoformed Plg are laths from 50 nm up to 300 nm in length. Although authigenic aluminum-rich Sep deposits are detected in Las Eras, the greater abundance of Plg compared to Sep could be linked to an increase in aluminum activity [58]. Unlike the well-preserved bundles of authigenic aluminium-rich Sep (Figure

10A,B) in Las Eras, the inherited magnesium Plg bundles (Figure 10C) exhibit degraded edges. Aluminum-rich Plg deposits are also of authigenic origin because they are laths and rods, straight, and rigid, with no signs of erosion and, in some cases, associated with Sme (Figure 8A). These Plg deposits are frequent in nature due to the transformation of Sme [43], and they could be the result of an epitaxial intergrowth with Sme [59]. Other authors have theorized about the transformation of Plg into Sme under alkaline pH and environmental conditions [60]. Clay mineral intergrowth between Sme and Plg has also been observed in Paleogene calcretes in Central Spain, where the transformation in the solid state is unlikely due to their structural differences [61].

Chl clay minerals are abundant in the Miocene layers but scarce or absent in the studied playa-lakes sediments (Figures 5, S1, and S2). The dissolution of Chl may explain this notable decrease. The dissolved Chl appears to be the most probable source of iron for iron-rich Plg exclusively detected in Caballo Alba. Thus, iron-rich Plg is of neoformed origin. The incongruent dissolution of Chl occurs at alkaline pH [62,63], whereas Plg precipitation is favored by high pH levels (8–9.5) and high Mg+Si/Al ratios [5]. The iron present in the form of $Fe^{2+}$ in the structure of Chl may oxidize to $Fe^{3+}$ in solution as a function of pH [64,65]. Thus, Plg neoformed in the Caballo Alba playa-lake should preferentially incorporate the available $Fe^{3+}$ in the solution. The authors of [66] carried out a Mössbauer characterization and concluded that iron in Plg is ferric and occupies M1 and M2 sites. Ref. [67] involving XRF studies revealed a very similar iron concentration between bulk samples of these Miocene rocks (av. 16.26%) and these playa-lake sediments (av. 16.7%). In addition, $Fe^{3+}$ is strongly correlated with other characteristic elements of clay minerals (e.g., $Si^{4+}$, $Al^{3+}$, $Ti^{4+}$, and $K^{+}$) [67]. The preferential incorporation of $Fe^{3+}$ into the structure of Plg is favored by the incorporation of $Mg^{2+}$ into authigenic saponite (Sap), which is abundant in Caballo Alba. The mean structural formula of these Sap is $[(Si_{3.35–4}Al_{00.0–0.65})\ O_{10}\ (Al_{0.18–1.70}\ Fe_{0.11–0.50}\ Mg\ _{0.27–2.12}\ Mn\ _{0.00–0.04}\ Ti\ _{0.00–0.08})\ (K_{0.00–0.61}\ Na\ _{0.00–0.27}\ Ca\ _{0.03–0.20})\ (OH)_2{\cdot}nH_2O]$ [30]. Beyond the scope of this study, Sap authigenesis is active in this lake and could involve also some Chl transformation into iron-rich Sme, in contrast to Las Eras and Bodón Blanco, where Sap is absent (Figures S1 and S2). This has a significant impact on the geochemical $Mg^{2+}$ correlation with clay-forming elements (e.g., $Si^{4+}$, $Al^{3+}$, $Ti^{4+}$, and $K^{+}$) in Caballo Alba in contrast to Las Eras, where it is absent [67].

Miocene calcitic/dolo-mudstone contains an assemblage of Sme and iron-rich Plg (Figure 4A) that is analog to the Caballo Alba clay mineral assemblage (Figure 7). As in modern deposits, the relative enrichment in $Fe_2O_3$ of Miocene Plg coincides with the Sme content of the montmorillonitic (Mnt) composition $[(Si_{3.54–4}\ Al\ _{0.00–0.46})\ O_{10}\ (Al_{0.69–1.59}\ Fe_{0.20–0.73}\ Mg_{0.21–0.73}\ Mn\ _{0.00–0.17}\ Ti\ _{0.00–0.07})\ (K_{0.12}\ Na_{0.00–0.18}\ Ca_{0.01–0.19})\ (OH)_2{\cdot}nH_2O]$ [30]. Our results suggest that Sap enables higher $Fe^{3+}$ uptake by Plg than Mnt (Figure 6). An association of iron-rich Plg and magnesium-rich Sap has been reported in the Neogene geological record of alkaline lakes [3]. The Plg fibers described by [3] comprised up to 1.05 Fe atoms p.h.u.c, whereas Caballo Alba iron-rich Plg reached 0.8 Fe atoms p.h.u.c. The proposed structural formulae $[(Si_7\ Al_1)\ O_{20}\ (Al_{0.57}\ Mg\ _{2.78}\ Fe\ _{0.8})\ (Ca_{0.21}\ K_{0.19}\ Na_{0.72})\ (OH)_2 \cdot (OH_2)_4{\cdot}4H_2O]$ fits with an iron-rich Plg (Table 1). Iron-rich Plg deposited in Caballo Alba provides insight into iron-rich Plg deposits that were analyzed elsewhere in [68] considering the Maderuelo deposit (i.e., up to 1.31 Fe atoms p.h.u.c) (Duero Basin, Spain); in [69] considering the Pefkaki deposit (i.e., up to 0.99 Fe atoms p.h.u.c) (Greece); and in [10] considering the Altillo Grande playa-lake (i.e., $x \geq 0.5$) (Guadiana Basin, Spain).

Table 1 presents the classification of studied Plg in Caballo Alba, according to [44]. These results are very similar to Plg reported in southern Iranian soils of Hormozgan province, where types III (i.e., trioctahedral Plg) and IV (i.e., aluminum-rich Plg) are the dominant Plg types and Type II is the minority [70], as in Caballo Alba. Nevertheless, the Iranian Plg deposits are mostly neoformed [70], whereas in the studied playa-lakes, they

are mostly inherited. Ref. [71] compared clay mineral assemblages in the Persian Gulf and the Gulf of Oman, and they found that Plg is more abundant in cores from the Iranian side of the Persian Gulf, reflecting the influence of Zagros hinterland. In the strait of Hormuz, Plg and Sme almost disappear, and in the Gulf of Oman, Mca and Chl are the dominant clay minerals [71]. In the NW side of the Persian Gulf, bordering Kuwait and Iraq coasts, Plg with no trend of distribution it is most probably derived from ancient Mesopotamian flood plain and submerged estuarine sediments of the Shatt-al-Àrab (i.e., Tigris and Euphrates rivers) transported by fluvial influxes and dust storms associated with NW winds (Shamal) [72,73].

The Plg present in calcretes and other sedimentary rocks associated with lacustrine or playa environments in continental settings can be of authigenic [74–76] or inherited origins [77]. The authigenic Plg of late Miocene–Pliocene lacustrine deposits of the Kızılırmak Formation (Kırsehir Region, Turkey) exhibit some similarities with aluminum-rich Plg of Caballo Alba and Bodón Blanco. The transformation of detrital Sme into fiber and fiber bundles of Plg represents a more evolved stage [74] than that observed for the studied playa-lakes (Figure 8A). This feature is evident in the aggregation stage of the fibers but not in the width of laths; there are some similarities in the widths ranging from 10 to 50 nm with laths of sharp edges [72], as shown in Figure 8. The dissolution–precipitation mechanism is proposed as the underlying process rather than the pure transformation of detrital Sme into Plg, as stated previously by [61,74]. In other sedimentary successions of Central Asia (i.e., Kazakhstan), the authigenic origin of Plg and its association with Sme in the Chu-Surasu Basin (late Cretaceous) [75] or Chl in the Bastau Formation (mid-Miocene) [76] points to the weathering process of igneous rocks under dry conditions. The detrital Plg deposits of calcretes of Thar Dessert (Rajasthan state, India) are inherited from marine sedimentary rocks of the area belonging to the Jaisalmer Formation (Cretaceous to Eocene age) related to aeolian flux during increased aridity over the last 30 ka in relation to fluctuating SW monsoonal strength [77]. In this same line, the abundance of detrital Plg in the studied hyperalkaline playa-lakes opens a window to potential paleoclimatic studies (i.e., aridity) along their sedimentary record.

## 6. Conclusions

The Caballo Alba, Las Eras, and Bodón Blanco hyperalkaline playa-lakes host a mixture of authigenic and detrital clay minerals that vary from lake to lake and differ from Miocene source rocks, with their precipitation dependent on slight differences in physicochemical conditions. Miocene marlstones and mudstones comprise an assemblage of Mca-Chl-Kln-Sep-Plg with Sme only present in the topmost mudstone. In contrast, in the three studied playa-lakes, the relative abundances of Sep and Chl are very low due to the dissolution effect by high pH waters. Alternatively, mineralogical, textural, and crystallochemical features indicate that Plg particles of different octahedral compositions precipitate in the three lakes. The concurrent authigenesis of Sme occur in Caballo Alba, in contrast to Las Eras and Bodón Blanco. Authigenic Plg occurs as the laths and rods with lengths of 50 nm and distinctively are enriched in one octahedral cation (MgO, $Al_2O_3$, and $Fe_2O_3$) depending on sedimentary conditions. Aluminum-rich Plg particles from the three playa-lakes could be intergrowth with Sme favored by high pH. Iron-rich Plg precipitates only in association with authigenic Sme (Sap) in the Caballo Alba playa-lake. In this case, Sme of Sap composition preferentially uptakes magnesium from the environment, and the available dissolved iron is mainly derived from Chl dissolution, due to its scarce presence in these playa-lakes. The same effect of magnesium competition between Sm and Plg is observed in a Miocene mudstone, where Plg is relatively enriched in iron. The exact conditions of Sm precipitation in some Miocene rocks should be constrained in future paleoenvironmental studies. Our findings in spatially close and hydrochemical equivalent

playa-lakes provide evidence that authigenic Plg-bearing mineral assemblages can be used as geochemical proxies. Future perspectives include unraveling the authigenic mechanisms of Sap in Caballo Alba and seeking to define more in-depth iron-rich and aluminum-rich Plg as well as Sep precipitation. An investigation of the relationship between arid conditions and detrital Plg deposited in playa-lakes during the Holocene is also pending.

**Supplementary Materials:** The following supporting information can be downloaded at: https://www.mdpi.com/article/10.3390/min15010050/s1, Table S1: Bulk mineralogy; semiquantification results obtained by XRD powder method of marlstones sampled from the Vallesian stratigraphic section. In yellow: Selected samples for clay mineralogy.; Table S2: Clay mineralogy. Semi-quantification results obtained by XRD oriented mounts method of Miocene marlstones and mudstones.; Table S3: Clay mineralogy. Semi-quantification results obtained by XRD oriented mounts method of Caballo Alba sediments.; Figure S1: XRD patterns of oriented mounts of a representative sample from Las Eras: air dried (AD), ethylene glycol solvated (EG) and thermal treated (TT) (550 °C). The clay mineral assemblage comprise: mica (Mca), palygorskite (Plg) and kaolinite (Kln).; Table S4: Clay mineralogy. Semi-quantification results obtained by XRD oriented mounts method of Las Eras sediments.; Figure S2: XRD patterns of oriented mounts of a representative sample from Bodón Blanco: air dried (AD), ethylene glycol solvated (EG) and thermal treated (TT) (550 °C). The clay mineral assemblage comprise: sepiolite (Sep), palygorskite (Plg), mica (Mca) and kaolinite (Kln).; Table S5: Clay mineralogy. Semi-quantification results obtained by XRD oriented mounts method of Bodón Blanco sediments.

**Author Contributions:** Conceptualization, P.d.B., M.E.S.-M. and J.P.R.-A.; methodology, J.P.R.-A., M.S.-R. and F.N.; software, F.N.; investigation, P.d.B., M.E.S.-M., J.P.R.-A. and M.S.-R.; writing—original draft preparation, P.d.B.; writing—review and editing, P.d.B., M.E.S.-M., J.P.R.-A.; M.S.-R. and F.N.; visualization, J.P.R.-A.; supervision, M.E.S.-M., J.P.R.-A.; M.S.-R. and F.N.; project administration, M.E.S.-M. and M.S.-R.; funding acquisition, M.E.S.-M. All authors have read and agreed to the published version of the manuscript.

**Funding:** This research was funded by the Spanish Ministry of Science and Innovation through the National Research Project PID2021-123735OB-C22 along with financial support from the Dutch Research Council project OCENW.KLEIN.037.

**Data Availability Statement:** Dataset available on request from the authors.

**Acknowledgments:** This project is part of the scientific activities of the Research Group UCM-910404 and Geobiology group at Vrije Universiteit Amsterdam. Pablo del Buey acknowledges support from a Predoctoral Grant (CT27/16-CT28/16 UCM) and a Postdoctoral Grant (Margarita Salas CT18/22) at Department of Earth Sciences at Vrije Universiteit Amsterdam and Department of Mineralogy and Petrology at University of Granada. Óscar Cabestrero Aranda is acknowledged for his assistance in the field. Finally, Esteban Urones Garrote (CNME-UCM) and Josefina Pedrajas Jurado (CIC-UGR) are acknowledged for their kind assistance with TEM-AEM analyses and images of Plg and Sep particles.

**Conflicts of Interest:** The authors declare no conflict of interest.

## References

1. Singer, A. Palygorskite in sediments: Detrital, diagenetic or neoformed—A critical review. *Int. J. Earth Sci.* **1979**, *68*, 996–1008.
2. Calvo, J.P.; Blanc-Valleron, M.M.; Rodríguez-Aranda, J.P.; Rouchy, J.M.; Sanz-Montero, M.E. Authigenic clay minerals in continental evaporitic environments. In *Palaeoweathering Palaeosurfaces and Related Continental Deposits*; Wiley: Hoboken, NJ, USA, 1999; Volume *27*, pp. 129–151.
3. Akbulut, A.; Kadir, S. The geology and origin of sepiolite, palygorskite and saponite in Neogene lacustrine sediments of the Serinhisar-Acipayam Basin, Denizli, SW Turkey. *Clays Clay Miner.* **2003**, *51*, 279–292.
4. Leguey, S.; Pozo, M.; Medina, J.A. Polygenesis of sepiolite and palygorskite in a fluvio-lacustrine environment in the Neogene basin of Madrid. *Mineral. Petrogr. Acta* **1985**, *29*, 287–301.
5. Jones, B.F.; Galán, E. Sepiolite and palygorskite. In *Hydrous Phyllosilicates*; Bailey, S.W., Ed.; Reviews in Mineralogy; Mineralogical Society of America: Washington, DC, USA, 1988; Volume 19, pp. 631–674.

6. Chen, T.; Xu, H.; Lu, A.; Xu, X.; Peng, S.; Yue, S. Direct evidence of transformation from smectite to palygorskite: TEM investigation. *Sci. China D Earth Sci.* **2004**, *47*, 985–994.
7. Singer, A.; Norrish, K. Pedogenic palygorskite occurrences in Australia. *Am. Mineral.* **1974**, *59*, 508–517.
8. Chahi, A.; Fritz, B.; Duplay, J.; Weber, F.; Lucas, J. Textural transition and genetic relationship between precursor stevensite and sepiolite in lacustrine sediments (Jbel Rhassoul, Morocco). *Clays Clay Miner.* **1997**, *45*, 378–389.
9. Miller, C.R.; James, N.P. Autogenic microbial genesis of middle Miocene palustrine ooids; Nullarbor Plain, Australia. *J. Sediment. Res.* **2012**, *82*, 633–647. https://doi.org/10.2110/jsr.2012.60.
10. Del Buey, P.; Cabestrero, Ó.; Arroyo, X.; Sanz-Montero, M.E. Microbially induced palygorskite-sepiolite authigenesis in modern hypersaline lakes (Central Spain). *Appl. Clay Sci.* **2018**, *160*, 9–21.
11. Suárez, M.; Robert, M.; Elsass, F.; Martín-Pozas, J.M. Evidence of *a* precursor in the neoformation of palygorskite—New data by analytical electron microscopy. *Clay Miner.* **1994**, *29*, 255–264.
12. Galán, E.; Ferrero, A. Palygorskite-sepiolite clays of Lebrija, Southern Spain. *Clays Clay Miner.* **1982**, *30*, 191–199.
13. Pozo, M.; Casas, J.C. Origin of kerolite and associated Mg clays in palustrine-lacustrine environments. The Esquivias deposit (Neogene Madrid Basin, Spain). *Clay Miner.* **1999**, *34*, 395–418.
14. Millot, G. *Geology of Clays*; Springer: London, UK, 1970; 429p.
15. Deocampo, D.M.; Cuadros, J.; Wing-Dudek, T.; Olives, J.; Amouric, M. Saline lake diagenesis as revealed by coupled mineralogy and geochemistry of multiple ultrafine clay phases: Pliocene Olduvai Gorge, Tanzania. *Am. J. Sci.* **2009**, *309*, 834–868.
16. Stoessell, R.K. 25°C and 1 atm. Dissolution experiments of sepiolite and kerolite. *Geochim. Cosmochim. Acta* **1988**, *52*, 365–373.
17. Deocampo, D.M. Evaporative evolution of surface waters and the role of aqueous $CO_2$ in magnesium silicate precipitation: Lake Eyasi and Ngorongoro crater, northern Tanzania. *S. Afr. J. Geol.* **2005**, *108*, 493–504.
18. Deocampo, D.M.; Blumenschine, R.J.; Ashley, G.M. Wetland diagensis and traces of early hominids, Olduvai Gorge, Tanzania. *Quat. Res.* **2002**, *57*, 271–281.
19. Cuevas, J.; Vigil de la Villa, R.; Ramírez, S.; Petit, S.; Meunier, A.; Leguey, S. Chemistry of Mg smectites in lacustrine sediments from the Vicálvaro sepiolite deposit, Madrid Neogene Basin (Spain). *Clays Clay Miner.* **2003**, *51*, 457–472.
20. Galán, E.; Pozo, M. Palygorskite and Sepiolite Deposits in Continental Environments. Description, Genetic Patterns and Sedimentary Settings. In *Developments in Palygorskite-Sepiolite Research. A New Outlook on these Nanomaterials*; Galán, E., Singer, A., Eds.; Elsevier: New York, NY, USA, 2011; Volume 3, pp. 125–166.
21. Fernández-Macarro, B.; Armenteros, L.; Blanco, J.A. Procesos de alteración y paleosuelos ligados a la sedimentación miocena del noreste de Segovia, Depresión del Duero. *Acta Geol. Hispánica* **1988**, *23*, 269–281.
22. Doval, M.; Domínguez, M.C.; Brell, J.M.; García, E. Mineralogía y sedimentología de las Facies distales del borde norte de la Cuenca del Tajo. *Bol. Soc. Esp. Mineral.* **1985**, *8*, 257–269.
23. Ordóñez, S.; Calvo, J.P.; García del Cura, M.Á.; Alonso-Zarza, A.M.; Hoyos, M. Sedimentology of sodium sulphate deposits and special clays from the Tertiary Madrid Basin (Spain). In *Lacustrine Facies Analysis*; Anadón, P., Cabrera, L., Kelts, K., Eds.; Special Publication International Association of Sedimentologists; Blackwell Scientific Publications: Oxford, UK, 1991; Volume 13, pp. 39–55.
24. García-Romero, E. Génesis de arcillas magnésicas en la cuenca de Madrid: Interrogantes planteados. *Bol. Geol. Miner.* **2004**, *115*, 629–640.
25. Murray, H.H.; Pozo, M.; Galán, E. An introduction to palygorskite and sepiolite deposits. Location, geology and uses. In *Developments in Palygorskite and Sepiolite Research. A New Outlook on These Nanomaterials*; Galán, E., Singer, A., Eds.; Elsevier: New York, NY, USA, 2011; Volume 3, pp. 85–100.
26. Sanz-Montero, M.E.; Rodríguez-Aranda, J.P.; Del Buey, P. Influencia del sustrato cenozoico en el origen y sedimentación de la laguna hiperalcalina de Caballo Alba (Segovia). *Geogaceta* **2021**, *70*, 31–34.
27. Alonso-Gavilán, G.; Armenteros, I.; Carballeira, J.; Corrochano, A.; Huerta, P.; Rodríguez, J.M. Cuenca del Duero. In *Geología de España*; Vera, J.A., Ed.; SGE-IGME: Madrid, Spain, 2004; pp. 550–556.
28. Portero, J.M.; Carreras, F.; Olivé, A.; Del Olmo, P. Mapa Geológico de España Escala 1:50.000, Hoja 428, Olmedo; IGME: Madrid, Spain, 1982.
29. Cabestrero, Ó.; Sanz-Montero, M.E. Brine evolution in two inland evaporative environments: Influence of microbial mats in mineral precipitation. *J. Paleolimnol.* **2018**, *59*, 139–157.
30. Del Buey, P. Interacciones Bióticas en la Neoformación de Minerales en Lagunas Salinas y Alcalinas, con Énfasis en los Minerales de la Arcilla. Ph.D. Thesis, Universidad Complutense de Madrid, Madrid, Spain, 2022.
31. Del Buey, P.; Sanz-Montero, M.E. Biomineralization of ordered dolomite and magnesian calcite by the green alga *Spirogyra*. *Sedimentology* **2022**, *70*, 685–704.
32. Sanz-Montero, M.E.; del Buey, P.; Cabestrero, Ó.; Sánchez-Román, M. Isotopic signatures of microbial Mg-carbonates deposited in an ephemeral hyperalkaline lake (Central, Spain): Paleoenvironmental implications. *Minerals* **2023**, *13*, 617. https://doi.org/10.3390/min13050617.
33. Sanz-Montero, M.E.; Cabestrero, Ó.; Sánchez-Román, M. Microbial Mg-Rich Carbonates in an Extreme Alkaline Lake (Las Eras, Central Spain). *Front. Microbiol.* **2019**, *10*, 148.
34. Chung, F.H. Quantitative interpretation of X-ray diffraction patterns. I. Matrix flushing method for quantitative multicomponent analysis. *J. Appl. Crystallogr.* **1974**, 7, 519–931.

35. Kübler, K. Cristallinité de L'illite, Méthodes Normalisées de Préparations, Méthodes Normalisées de Mesure; Série ADX; Cahiers Institut de Geologie: Neuchâtel, Switzerland, 1987; 13p.
36. Nieto, F.; Arroyo, X.; Aróstegui, J. XRD-TEM-AEM comparative study of n-alkilamonnium smectites and interestratified minerals in shallow-diagenetic carbonate sediments of the Basque-Cantabrian Basin. *Am. Mineral.* **2016**, *101*, 385–398.
37. Jackson, M.L. *Soil Chemical Analysis Advanced Course*; CABI Digital Library: Madison, WI, USA, 1969; 895p.
38. Warr, L.N. IMA-CNMNC approved mineral symbols. *Mineral. Mag.* **2021**, *85*, 291–320. https://doi.org/10.1180/mgm.2021.43.
39. Yebra, Á. Influencia de la Mineralogía, Quimismo y Textura en las Aplicaciones Básicas Industriales de la Sepiolita. Ph.D. Thesis, Universidad de Granada, Granada, Spain, 2000.
40. Cliff, G.; Lorimer, G.W. The quantitative analysis of thin specimens. *J. Microsc.* **1975**, *103*, 203–207.
41. Elert, K.; Nieto, F.; Azañon, J.M. Effects of lime treatments on marls. *Appl. Clay Sci.* **2017**, *135*, 611–619.
42. García-Romero, E.; Suárez, M. Sepiolite-palygorskite: Textural study and genetic considerations. *Appl. Clay Sci.* **2013**, *86*, 129–144.
43. Suárez, M.; García-Romero, E. Sepiolite-palygorskite: A continous polysomatic series. *Clays Clay Miner.* **2013**, *61*, 461–472.
44. García-Romero, E.; Súarez, M. On the chemical composition of sepiolite and palygorskite. *Clays Clay Miner.* **2010**, *58*, 1–20.
45. Velde, B. Composition and mineralogy of clay minerals. In *Origin and Mineralogy of Clays*; Velde, B., Ed.; Springer: New York, NY, USA, 1995; pp. 8-42.
46. Neaman, A.; Singer, A. The effects of palygorskite on chemical and physico-chemical properties of soils: A review. *Geoderma* **2004**, *123*, 297–303. https://doi.org/10.1016/j.geoderma.2004.02.013.
47. Muir, A. Notes on the soils of Syria. *Eur. J. Soil. Sci.* **1951**, *2*, 163–182.
48. Rogers, L.E.R.; Quirk, J.P.; Norrish, K. Ocurrence of an aluminum sepiolite in a soil having an unusual water relationships. *J. Soil. Sci.* **1956**, *7*, 177–185.
49. Singer, A. The texture of palygorskite from the Rift Valley, southern Israel. *Clay Miner.* **1981**, *16*, 415–419.
50. Ravikovitch, S.; Pines, F.; Ben-Yair, M. Composition of colloids in soils of Israel. *J. Soil. Sci.* **1960**, *11*, 82–91.
51. McLean, S.A.; Allen, B.L.; Craig, J.R. The occurrence of sepiolite and attapulgite on the southern High Plains. *Clays Clay Miner.* **1972**, *20*, 143–149.
52. Shadfan, H.; Mashhady, A.S. Distribution of palygorskite in sediments and soils of Eastern Saudi Arabia. *Soil Sci. Soc. Am. J.* **1985**, *49*, 243–250.
53. Cui, J.; Zhang, Z.; Han, F. Effects of pH on the gel properties of montmorillonite, palygorskite and montmorillonite-palygorskite composite clay. *Appl. Clay Sci.* **2020**, *190*, 105543. https://doi.org/10.1016/j.clay.2020.105543.
54. Martínez-Ramirez, S.; Puertas, F.; Blanco-Varela, M.T. Stability of sepiolite in neutral and alkaline media at room temperature. *Clay Mineral.* **1996**, *31*, 225–232.
55. Grim, R.E. *Clay Mineralogy*; Mc Graw-Hill: New York, NY, USA, 1968**.**
56. Hodge, T.; Turchenek, L.W.; Oades, J.M. Ocurrence of palygorskite in ground water rendzinas (petrocalcic Calciaquolls) in Southeast South Australia. In *Palygorskite-Sepiolite: Occurrences, Genesis and Uses*; Developments in Sedimentology; Elsevier: Amsterdam, The Netherlands, 1984; Volume 37, pp. 199–210.
57. Verrechia, E.P.; Le Coustumer, M.N. Occurrence and genesis of palygorskite and associated clay minerals in a Pleistocene calcrete complex, Sde Boquer, Negev desert, Israel. *Clay Mineral.* **1996**, *31*, 183–202.
58. Birsoy, R. Formation of sepiolite-palygorskite and related minerals from solution. *Clays Clay Miner.* **2002**, *50*, 736–745.
59. Krekeler, M.P.S.; Hammerley, E.; Rakovan, J.; Guggenheim, S. Microscopy studies of the palygorskite to smectite transformation. *Clays Clay Miner.* **2005**, *53*, 92–99.
60. Golden, D.C.; Dixon, J.B.; Shadfan, H.; Kippenberger, L.A. Palygorskite and sepiolite alteration to smectite under alkaline conditions. *Clays Clay Miner.* **1985**, *33*, 44–50.
61. Rodas, M.; Luque, F.J.; Mas, R.; Garzón, M.G. Calcretes, palycretes and silcretes in the Paleogene detrital sediments of the Duero and Tajo Basins, Central Spain. *Clay Mineral.* **1994**, *29*, 273–285.
62. Malmström, M.; Banwart, S.; Lewenhagen, J.; Duro, L.; Bruno, J. The dissolution of biotite and chlorite at 25°C in the near-neutral pH region. *J. Contam. Hydrol.* **1996**, *21*, 201–213.
63. Rochelle, C.A.; Bateman, K.; MacGregor, R.; Pearce, J.M.; Savage, D.; Wetton, P.D. Experimental determination of chlorite dissolution rates. *MRS Online Proc. Lib.* **1996**, *353*, 149–156.
64. Stumm, W.; Morgan, J.J. *Aquatic Chemistry*; Wiley-Interscience: New York, NY, USA, 1996.
65. Lowson, R.T.; Josick-Comarmond, M.C.; Rajaratnam, G.; Brown, P.L. The kinetics of dissolution of the chlorite as a function of pH and at 25°C. *Geochim. Cosmochim. Acta* **2005**, *69*, 1687–1699. https://doi.org/10.1016/j.gca.2004.09.028.
66. Huang, Y.J.; Li, Z.; Li, S.Z.; Shi, Z.L.; Yin, L.; Hsia, Y.F. Mössbauer investigations of palygorskite from Xuyi, China. *Nucl. Instrum. Methods Phys. Res. Sect. B Beam Interact. Mater. Atoms* **2007**, *260*, 657–662. https://doi.org/10.1016/j.nimb.2007.04.218.
67. Grunwald, C. Estudio geoquímico de depósitos lagunares en la Cuenca del Duero con énfasis en la distribución del arsénico. Master's Thesis, Universidad Complutense de Madrid, Madrid, Spain, 2024**.**
68. Torres-Ruíz, J.; López-Galindo, A.; González-López, J.M.; Delgado, A. Geochemistry of Spanish sepiolite-palygorskite deposits: Genetic considerations based on trace elements and isotopes. *Chem. Geol.* **1994**, *112*, 221–245.
69. Chryssikos, G.D.; Gionis, V.; Kacandes, G.H.; Statopoulou, E.T.; Suárez, M.; García-romero, E.; Sánchez del Río, M. Octahedral cation distribution in palygorskite. *Am. Mineral.* **2009**, *94*, 200–203.

70. Abbaslou, H.; Abtahi, A.; Martin Peinado, F.J.; Owliaie, H.; Khormali, F. Mineralogy and characteristic of soils developed on Persian Gulf and Oman Sea basin, southern Iran: Implications for soil evolution in relation to sedimentary parent material. *Soil Sci.* **2013**, *178*, 568–584. https://doi.org/10.1097/SS.0000000000000022.
71. Stoffers, P.; Ross, D.A. Late Pleistocene and Holocene sedimentation in the Persian Gulf-Gulf of Oman. *Sediment. Geol.* **1979**, *23*, 181–208.
72. Al-Bakri, D.; Khalaf, F.; Al-Ghadban, A. Mineralogy, genesis, and sources of surficial sediments in the Kuwait marine environment, northern Arabian Gulf. *J. Sed. Petrol.* **1984**, *54*, 1266–1279.
73. Aqrawi, A.A.M. Petrography and mineral content of sea-floor sediments of the Tigris-Euphrates Delta, North-West Arabian Gulf, Iraq. *Estuar. Coast. Shelf. Sci.* **1994**, *38*, 569–582.
74. Kadir, S.; Eren, M.; Külah, T.; Önalgil, N.; Cesur, M.; Gürel, A. Genesis of Late Miocene-Pliocene lacustrine palygorskite and calcretes from Kirsehir, central Anatolia, Turkey. *Clay Mineral.* **2014**, *49*, 473–494. https://doi.org/10.1180/claymin.2014.049.3.09.
75. Munara, A.; Cathelineau, M.; Carpentier, C.; Abylay, N. Clays as indicator of paleoclimate and source rocks in The Chu-Sarysu Basin (Kazakhstan). Kazakhstan *J. Oil Gas Ind.* **2023**, *5*, 21–35. https://doi.org/10.54859/kjogi108603.
76. Voigt, S.; Weber, Y.; Frisch, K.; Barteinstein, A.; Hellwing, A.; Petschick, R.; Bahr, A.; Pross, J.; Koutsodendris, A.; Voigt, T. Climatically forced moisture supply, sediment flux and pedogenesis in Miocene mudflat deposits of south-east Kazakhstan, Central Asia. *Depos. Rec.* **2017**, *3*, 209–232. https://doi.org/10.1002/dep2.34.
77. Hameed, A.; Raja, P.; Ali, M.; Upreti, N.; Kumar, N.; Tripathi, J.K.; Srivastava, P. Micromorphology, clay mineralogy, and geochemistry of calcic-soils from western Thar Desert: Implications from origin of palygorskite and southwestern monsoonal fluctuations over the last 30 ka. *Catena* **2018**, *163*, 378–398. https://doi.org/10.1016/j.catena.2017.12.034.